

## The Sphere of Influence of the Brightest Cluster Galaxies in the Diffuse Light of SDSS Clusters

Xiaokai Chen<sup>1</sup>, Ying Zu<sup>1,2\*</sup>, Zhiwei Shao<sup>1</sup>, Others

<sup>1</sup>Department of Astronomy, School of Physics and Astronomy, Shanghai Jiao Tong University, Shanghai 200240, China

<sup>2</sup>*Shanghai Key Laboratory for Particle Physics and Cosmology, Shanghai Jiao Tong University, Shanghai 200240, China*

Accepted XXX. Received YYY; in original form ZZZ

## ABSTRACT

**Key words:** galaxies: evolution — galaxies: formation — galaxies: abundances — galaxies: statistics — cosmology: large-scale structure of Universe

1 INTRODUCTION

The intracluster cluster light (ICL) is primarily produced by stray stars that are unassociated with any galaxies but still gravitationally bound to the cluster potential ([citation needed](#)) ([Zwicky 1937, 1952](#)), see recent review in ([Contini 2021](#)). As the by-product of galaxy interactions within clusters, these free-floating stars are key to unlocking the assembly history of the brightest cluster galaxies (BCGs) with future deep imaging surveys like the Chinese Space Station Telescope (CSST) ([citation needed](#)) ([Gong et al. 2019](#)), the Nancy Grace Roman Space Telescope (*Roman*) ([citation needed](#)) ([Spergel et al. 2015; Akeson et al. 2019](#)), and the Vera C. Rubin Observatory Legacy Survey of Space and Time (LSST) ([citation needed](#)) ([Ivezic et al. 2019](#)). However, it is unclear whether there exists an ICL component that is physically distinct from the diffuse stellar envelope of the BCG ([citation needed](#)) ([Kluge et al. 2021](#)), and if so, where the ICL begins and the sphere of influence of the BCG ends. In this paper, we examine the BCG+ICL stellar surface mass profile  $\Sigma_*^{B+I}$  of a large sample of SDSS clusters at  $0.2 < z < 0.3$ , in hopes of finding a more physically-motivated method of decomposing the  $\Sigma_*^{B+I}$  profile and the BCG “sphere of influence” within the diffuse cluster light.

In hydrodynamical simulations, methods for the kinematic decomposition of the BCG vs. ICL have been developed based on the apparent bimodal distribution of the velocities of intracluster stars ([citation needed](#)) ([Dolag et al. 2010](#); [Puchwein et al. 2010](#); [Cui et al. 2014](#)). However, such exquisite method developed for simula-

tions is not applicable in the observations, where stellar velocities are inaccessible (but see Gu et al. 2020(citation needed)(Gu et al. 2020)). As a result, traditional methods of decomposition usually assume that the diffuse light below some arbitrary surface brightness (SB) limit belongs to the ICL (citation needed)(Rudick et al. 2011; Burke et al. 2012; Presotto et al. 2014; Tang et al. 2018; Furnell et al. 2021), or describe the BCG+ICL SB profile  $\mu^{B+I}$  as the sum of multiple *seric* components (citation needed)(Gonzalez et al. 2005; Seigar et al. 2007; Donzelli et al. 2011; Cooper et al. 2015; Zhang et al. 2019; Montes et al. 2021). For example, describe a couple important papers that adopted the two aforementioned methods of separating BCG vs. ICL. I remember sending you a recent paper that did a review of this subject. (Gonzalez et al. 2005) investigate the surface brightness distribution surrounding BCGs in a 24 cluster sample at  $0.03 \leq z \leq 0.13$  and find that these surface brightness profiles are well described by a 2-deV model, which simply reproduces the observed position angle and ellipticity gradients. The inner component has a similar range of radii and axis ratios to typical massive elliptical galaxies and is associated with the BCG. Meanwhile, the outer part is more like the ICL population with a wider spatial distribution and steeper surface brightness gradient. (Furnell et al. 2021) estimate the ICL mass fraction of 18 clusters using *i* band image of the deep Hyper Suprime-Cam Subaru Strategic Programme (HSC-SSP) data release. By applying a rest-frame  $\mu_B=25$  mag/arcsec<sup>2</sup>, they find that  $\sim 24$  percent of total cluster stellar mass are residing in the ICL on average, and an obvious increase of ICL flux between  $0.1 \leq z \leq 0.5$ . Their finding implies that ICL derives the stellar mass evolution of clusters since  $z \sim 1$ . However, separating ICL from BCG directly

\* E-mail: yingzu@sjtu.edu.cn

based on surface brightness cut may introduce systematic effects on estimations like mass or light fraction both the ICL and BCG component obviously (like Fig. 8 of (Furnell et al. 2021)). Modeling the light profiles of the BCG and ICL with analytic models may provide excellent measurement on properties i.e. spatial distribution, but the results may be biased due to differences among samples (like (Gonzalez et al. 2005) discussion for specific BCG measurement). Despite the incoming deep photometric dataset from surveys like the *CSST*, a well-defined physical decomposition of the BCG+ICL profile is still lacking.

Recently, several studies proposed that the ICL in the outer region of clusters should follow the distribution of dark matter, due to the fact that the stray stars and dark matter particles are both collisionless tracers of the cluster potential (citation needed)(Montes & Trujillo 2019; Alonso Asensio et al. 2020; Poliakov et al. 2021) . By the same token, the outer ICL may also follow the distribution of satellite galaxies, whose mass loss contributes significantly to the ICL (citation needed)(Purcell et al. 2007; Martel et al. 2012; Contini et al. 2014; Morishita et al. 2017) . In this paper, we not only measure the BCG+ICL stellar surface mass density profile  $\Sigma_*^{B+I}$  from image stacking, but also the total surface mass density profile  $\Sigma_m$  from cluster weak lensing, as well as the galaxy surface number density profile  $\Sigma_g$  from cluster-galaxy cross-correlation. Informed by the observed distributions of dark matter and satellite galaxies within clusters, we develop a physically-motivated method for the decomposition of the diffuse stellar mass profile  $\Sigma_*^{B+I}$ .

In theory, since the intracluster stars are unlikely born *in situ* (citation needed)(Melnick et al. 2012) , the build-up of the diffuse light should be closely linked to the dynamical evolution of the BCG and satellite galaxies, including: (1) mergers of satellites with the BCG (citation needed)(Murante et al. 2007; Conroy et al. 2007; Burke et al. 2015) , (2) tidal disruption/stripping of satellites in the central region of the cluster (citation needed)(Montes & Trujillo 2014; DeMaio et al. 2015; Montes & Trujillo 2018; DeMaio et al. 2018; Contini et al. 2018) , (3) tidal and ram-pressure stripping of infalling satellites (citation needed)(Rudick et al. 2009; Contini et al. 2014, 2019; Jiménez-Teja et al. 2018, 2019) , and (4) pre-processing within infalling groups (citation needed)(Willman et al. 2004; Mihos et al. 2005; Rudick et al. 2006; Mihos et al. 2017; Han et al. 2018) . Among these processes, (1) and (2) can simultaneously grow the BCG and the ICL within a Hubble time, while (3) and (4) deposit stars only into the ICL without growing the BCG. In particular, the amount of ICL growth through (1) and (2) should be strongly correlated with the observed BCG stellar mass  $M_*^{BCG}$ , but the ICL growth induced by (3) and (4) would be tied instead to the number of satellite galaxies within the cluster (a.k.a., cluster richness  $\lambda$ ).

Therefore, we expect at least two physically distinct origins of the diffuse light, one *BCG-induced* and the other *richness-induced*. Obviously, the radial extent of the BCG-induced portion can be regarded as the radius of the BCG sphere of influence  $R_{SOI}$  within the diffuse cluster light. In this paper, we divide clusters into high and low- $M_*^{BCG}$  subsamples at fixed  $\lambda$  (see also Zu et al. 2021b, hereafter referred to as Z21), and infer  $R_{SOI}$  by comparing the  $\Sigma_*^{B+I}$  profiles between the two. Using weak lensing, Z21 found that the average halo concentration of the high- $M_*^{BCG}$  clusters is  $\sim 10\%$  higher than that of the low- $M_*^{BCG}$  clusters, but their average halo masses are the same. Since the two populations have the same  $\lambda$  (and average halo mass) but differs only in  $M_*^{BCG}$ , we expect their  $\Sigma_*^{B+I}(R)$  profiles to have equal richness-induced contributions beyond  $R_{SOI}$ , but exhibit distinct levels of BCG-induced diffuse mass below  $R_{SOI}$  — a potentially smoking-gun detection of  $R_{SOI}$ .

This paper is organised as follows. We provide an overview of the

cluster catalogue and photometric images in §2, setting the stage for our BCG+ICL SB profile measurement pipeline in §3. We describe the measurement and the decomposition of the BCG+ICL stellar surface density profile  $\Sigma_*^{B+I}$  in §4, and then present the observational detection of the BCG sphere of influence in §5. We conclude by summarizing our findings and looking to the future in §6. Throughout the paper, we assume the *Plank 2015* cosmology with  $\Omega_m = 0.31$ ,  $\sigma_8 = 0.816$ , and  $h = 0.6774$  (citation needed)(Planck Collaboration et al. 2016) , and convert all distances into physical coordinates. We use  $\lg x = \log_{10} x$  for the base-10 logarithm and  $\ln x = \log_e x$  for the natural logarithm.

## 2 DATA

### 2.1 Cluster Catalogue

Following Z21, we employ the SDSS redMaPPer cluster catalogue derived by applying a red-sequence-based cluster finding algorithm to the SDSS DR8 imaging (citation needed)(York et al. 2000; Aihara et al. 2011; Rykoff et al. 2014) . Briefly, redMaPPer iteratively self-trains a model of red-sequence galaxies calibrated by an input spectroscopic galaxy sample, and then attempts to grow a galaxy cluster centered about each photometric galaxy. Once a galaxy cluster has been identified by the matched-filters, the algorithm iteratively solves for a photometric redshift based on the calibrated red-sequence model, and re-centres the clusters about the best BCG candidates with the highest probability of being the central galaxy  $p_{cen}$  (citation needed)(Rykoff et al. 2014) .

For each detected cluster, redMaPPer applies an aperture of  $\sim 1 h^{-1}\text{Mpc}$  (with a weak dependence on satellite richness), and assign each galaxy within the aperture a membership probability  $p_{mem}$ . The satellite richness  $\lambda$  was computed by summing the  $p_{mem}$  of all member galaxy candidates, which roughly corresponds to the number of red-sequence satellite galaxies brighter than  $0.2 L_*$ . At  $\lambda \geq 20$ , the SDSS redMaPPer cluster catalogue is approximately volume-complete up to  $z \approx 0.33$ , with cluster photometric redshift uncertainties as small as  $\delta(z) = 0.006/(1+z)$ . We select 2440 clusters with  $\lambda \geq 20$  and redshifts between 0.2 and 0.3 ( $\langle z \rangle = 0.253$ ). The maximum redshift of 0.3 is primarily set by the requirement of sample completeness, and partly because the cosmic dimming effect renders the detection of low-SB signals within SDSS extremely challenging at the higher redshift ( $\mu \propto (1+z)^{-4}$ ).

We pick the galaxy with the highest  $p_{cen}$  in each cluster as the BCG, and derive an *i*-band cModel magnitude-based stellar mass  $M_*^{BCG}$  for each BCG. In general, the SDSS model magnitudes are preferred for measuring the color of extended objects like the BCGs (hence a better mass-to-light ratio indicator), because flux is measured consistently through the same aperture across all bands, while the cModel magnitudes provide a more robust estimate of the total flux based on independent model fits in each bandpass. Therefore, we rescale the extinction-corrected *gri* model magnitudes to the *i*-band cModel magnitudes, and fit a two-component Simple Stellar Population (SSP) template to the scaled *gri* magnitudes to infer  $M_*^{BCG}$ .

Following Maraston et al. 2009 (citation needed)(Maraston et al. 2009) , we assume a simultaneous burst of two SSPs at the same epoch, one dominant stellar population (97 per cent) with solar metallicity and the other a secondary (3 per cent) metal-poor ( $Z=0.008$ ) population. We utilize the EzGal software (Mancone et al. 2012 (citation needed)(Mancone & Gonzalez 2012) ) and adopt the BC03 SSP model and the Chabrier IMF for the fits. For a detailed comparison

between our photometric stellar mass estimates and the spectroscopic stellar masses from Chen et al. 2012 (citation needed)(Chen et al. 2012), we refer interested readers to the Figure 1 in Z21.

Due to the magnitude rescaling, our estimates of  $M_*^{\text{BCG}}$  should inherit the effective aperture of the  $i$ -band cModel magnitudes  $R_*$ . By examining the stacked surface stellar mass density profiles of clusters at fixed  $M_*^{\text{BCG}}$  but different  $\lambda$  (as will be demonstrated later in §5), we find that the effective aperture of our  $M_*^{\text{BCG}}$  estimates is  $R_* \approx 50$  kpc. Therefore, our measured  $M_*^{\text{BCG}}$  roughly corresponds to  $M_{*,50\text{kpc}}$  in the language of Huang et al. 2021 (citation needed)(Huang et al. 2021). To test the robustness of our  $R_{\text{SOI}}$  detection, we also compute for each BCG an aperture stellar mass  $M_{*,20\text{kpc}}$ , i.e., stellar mass enclosed within an aperture of 20 kpc.

## 2.2 SDSS Images

For any given set of clusters, we stack their SDSS images centred on the BCGs and measure the average 1D SB profile from the stacked 2D image. In this paper, we employ the observed images derived from the SDSS DR8, the same imaging data from which the redMaPPer cluster catalogue was built. **are you sure it is DR12? The SDSS imaging survey ends at DR8 It is DR8.** The images were processed with the latest SDSS photometric pipeline **photo** version v5\_6 need explicit name and version number of the software, which implements an updated sky subtraction method that significantly improves the flux estimates for bright objects, detection of faint objects around bright objects, and extended light measurement of large objects(Blanton et al. 2011). **Cite the Blanton paper** In particular, we make use of the “corrected frames”use proper quotation marks in LaTeX, i.e., the calibrated and sky-subtracted images (with bad columns and cosmic rays interpolated over**removed or interpolated over?** interpolated over, §3.1 in Blanton paper). Each corrected frame has a dimension of 2048 pixel  $\times$  1489 pixels, which corresponds to an angular size of  $13.5 \times 9.8$  arcmin<sup>2</sup> (the pixel size is 0.396 arcsec)**shouldn't those numbers be fixed and exact? Why did you use ~?.It should be! I just ignore the tail numbers, thus use ‘sim’** The improved photometric reduction of the SDSS images allows a robust measurement of the large-scale, diffuse light distribution within massive clusters, which was severely underestimated in the previous SDSS photometric pipeline (Bernardi et al. 2013; Kravtsov et al. 2018) . **cite the Kravtsov and Bernardi papers.**

Since the stacked measurement of the outer ICL is very sensitive to image quality, we apply a two-step procedure to identify the defect images. In the first step, we perform visual inspection of each image to look for strong defects that could severely undermine the stacked signal across all scales, e.g., extremely bright stars (and their extended bright wings) and strong cosmic rays across the frame. In the second step, we develop a simple  $\sigma$ -clipping scheme to reject some mildly defective images that could still impair our capability of detecting the faint ICL on scales larger than a few hundred kpc. In particular, we divide each image frame (after masking out all the galaxies, bright stars, and saturated pixels; described further below) into 70 200-pixel $\times$ 200-pixel cells (The pixel near the edge will be directly merged into the nearest cell, so the cell size of the last row and the last column will be larger than 200), and measure the average pixel flux ( $\bar{f}_{\text{cell}}$ ) within each cell. In addition, we measure the mean ( $\bar{f}_{\text{img}}$ ) and scatter ( $\sigma$ ) of the average fluxes of the 70 cells, and compute the deviation of the average flux of each cell from the mean flux of the entire image as  $\Delta f \equiv |\bar{f}_{\text{cell}} - \bar{f}_{\text{img}}|$ . We consider any image that includes a large block of  $M$  connected cells with  $\Delta f > N\sigma$  to be a potential contaminant. After extensive convergence tests, we find that the combination of  $M=5$  and  $N=6$  provides an robust selection

criteria for culling out bright extended features of non-cluster origin. In total, we identify 1466 strongly and 1690 mildly defective images from all three bands and exclude them from further stacking analysis.

## 3 SURFACE BRIGHTNESS PROFILE

To measure the BCG+ICL SB profiles  $\mu^{\text{B+I}}$  via image stacking, we mask out the bright stars and non-BCG galaxies (i.e., satellites and background galaxies) from each image, and then transform all the images from the cluster redshifts to the same reference redshift of  $z_{\text{ref}}=0.25$  (with the same pixel size but different image sizes).

Our method of measuring the diffuse light via image stacking is largely similar to that of (Zibetti et al. 2005, hereafter referred to as Z05), learn the **citatalias command I applied earlier,Done!** but with two important distinctions. Firstly, we directly utilize the sky-subtracted corrected frames for our SB measurements, while Z05 performed an independent sky subtraction on images in the SDSS Early Data Release. We have tested the Z05 sky-subtraction method on the raw DR8 SDSS images and find that the Z05 method generally produces consistent results compared to the SDSS pipeline. Secondly, we estimate the background level of the SB profiles, primarily due to undetected background galaxies and foreground stars, by stacking the real SDSS images centred on the coordinates of redMaPPer random clusters, while Z05 inferred the background SB by extrapolating from the best-fitting projected Navarro-Frenk-White (NFW) (citation needed)(Navarro et al. 1996) profile of the SB measurement below 900 kpc. We describe each step of our SB measurement in turn below.

### 3.1 Image Masking

**Present version:** For each image frame, we query the full width at half maximum (FWHM) of all stars brighter than  $m_r=20$  within  $\sim 12.53\text{arcmin}$  (1.5 half diagonal length of the image frame) around the center of the frame. We also query saturated pixels in each frame within the same query region. Next, we select stars that have FWHM measurement in at least one of the other two bands, and apply a mask with a diameter of  $30\times$  the maximum FWHM among the three bands. For saturated pixels, we increase the diameter of the masks to  $75\times$ FWHM in each band. We drop the stars fainter than  $m_r=20$  to minimize the impact of the foreground signal on our ICL measurement (Z05). Moreover, stars fainter than 20 mag have no obvious impact on surrounding pixels and have no good photometric measurement as those bright stars. If we apply the mask on these faint stars, surrounding pixels with ICL signal surrounding may be removed, which will introduce extra uncertainty in our ICL measurement. Even if the effects of those faint stars are non-negligible, we expect that the effects of these faint stars can be systematically removed by our background subtraction, in which we apply the same image processing as the cluster catalog on images matched with the redMaPPer random cluster catalog.

**Previous version:** For any star brighter than  $m_r=20$ , and have the full width at half maximum (FWHM) measured in at least one of the other two bandsWhy in at least two? and what about those stars that only have FWHM measured in r band only? When I did the star masking, I just follow the measurement limit for stars in Z05. They don't mention why apply this limit. I think this limit is to make sure these stars are a real objects. I don't know how it will be if I use stars observed in one specific band only., we measure the maximum FWHM (full width at half maximum) of the three bands and adopt  $30\times$ FWHM as the diameter of its mask. For very bright stars surrounded by a large number of saturated pixelshow did you

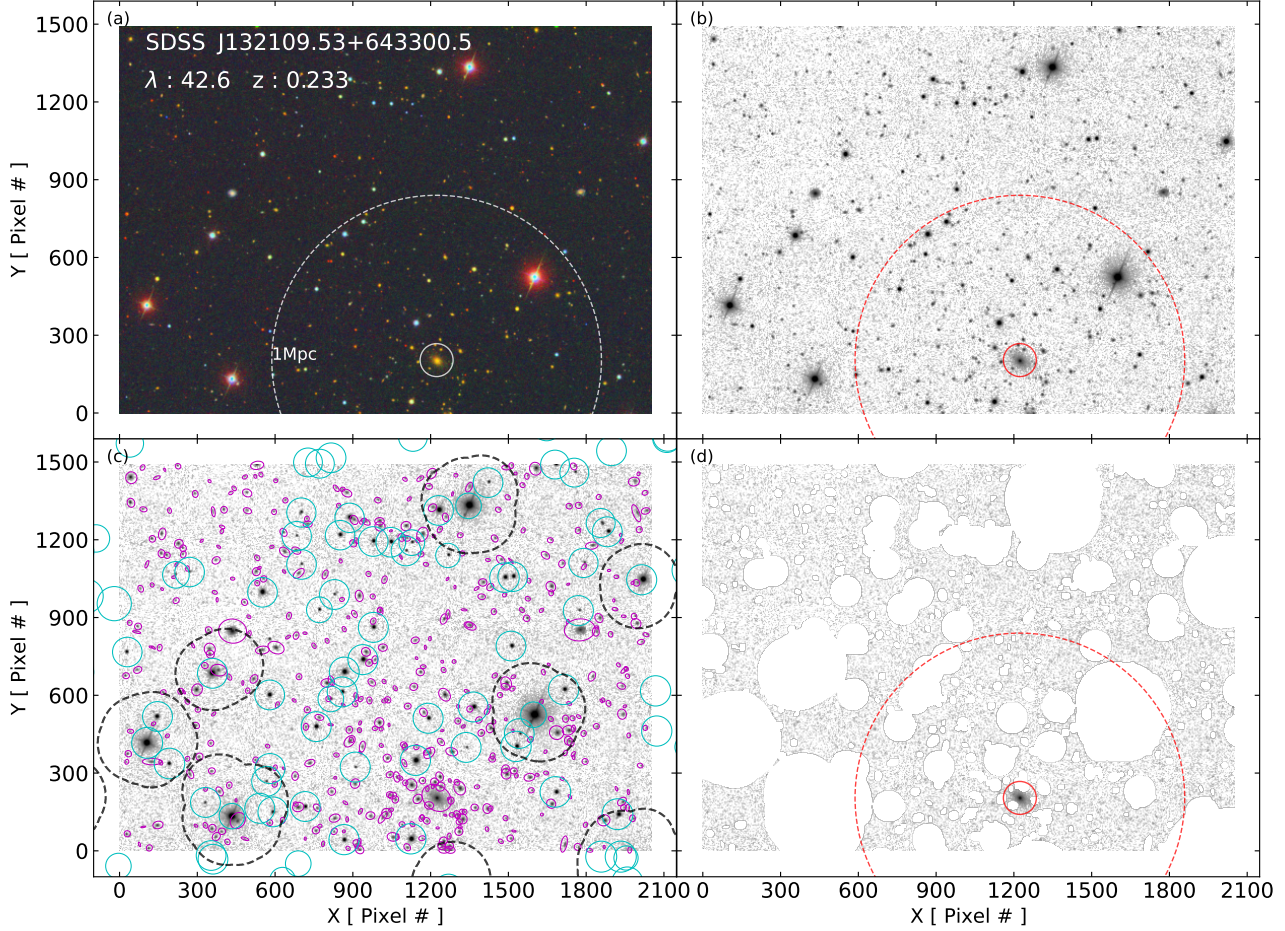


**Figure 1.** Example of star and galaxy masks on the standard SDSS image frame ( $589 \times 811 \text{ arcsec}^2$ ) of a cluster with  $\lambda=42.6$  at  $z = 0.233$ .  
 42.611 to 42.6, and is the redshift 0.233 or 0.245? Done! The image dimension is 2048 pixels by 1489 pixels, and the white margin area between the image boundary and the panel edge has a width of 100 pixels. Panel (a): SDSS *gri*-band composite image of the cluster, with its BCG indicated by the inner solid circle with a radius of 100kpc. The outer dotted circle indicates the cluster region of 1Mpc radius. Panel (b): The SDSS *r*-band image frame. Panel (c): Cyan circles and magenta ellipses are the star and galaxy masks, respectively, while the regions delineated by black dashed lines are the merged masks of saturated pixels. Note that we also include the masks of sources that are centred in the white margin area (i.e., outside but close to the image boundary), as they could still contaminate the pixels inside the image frame. Panel (d): Final masked image that only includes the light from the BCG, ICL, and unmasked sources that are below the detection threshold.

identify those stars? by what quantitative criteria? This is a mistake, I do not identify those bright stars, I just located saturated pixels surrounding them, and the mask size is applied on saturated pixels we increase the diameter of the masks to  $75 \times \text{FWHM}$ .

Previous version: According to Z05, this magnitude limit ensures that stars are masked unlikely to be misclassified galaxies. this sentence does not scan. Stars fainter than 20mag would have no systematic effect on ICL measurement due to their random location in the image frames, except the impacts on the signal fluctuation. This explanation is problematic. Both the bright and faint stars are random on the sky.

We have extensively tested the impact of different mask sizes on the measured BCG+ICL SB profile, and verified that our choices yield the best combination of signal-to-noise ratio (S/N) and star light mitigation.

For the galaxy masks, we run SExtractor<sup>1</sup> (citation needed) (Bertin & Arnouts 1996) on the cluster images in three

bands separately, using a detection threshold of  $1.5\sigma$  and a minimum detection area of five pixels. Such detection criteria result in a limiting magnitude of roughly 22.08 in the *i* band (i.e., absolute magnitude of -18.49 at  $z=0.25$ ), XXX Here I don't find the detection limit for extended sources. The 21 mag is  $10-\sigma$  detection limit for galaxies such that the magnitude error for faintest objects is  $\sim 0.1$  deeper than the nominal SDSS detection limit for extended sources. We multiply the semi-major and semi-minor radii of the ellipses detected by SExtractor by a factor of eight, and adopt the augmented ellipses as the masks for galaxies. We include the BCGs in the masks for the image selection described in §2.2, but leave them unmasked in the stacked profile measurements. The factor of eight is a relatively conservative choice, which ensures that we remove all the light physically associated with the satellite galaxies and the scattered light from some of the very bright, nearby galaxies.

To further remove any contamination induced by bright stars and

<sup>1</sup> We use SExtractor version 2.25.0 throughout the present work.

<sup>2</sup> Data model of profMean: <https://www.sdss.org/dr12/algorithms/magnitudes/>.

<sup>3</sup> SDSS Schema Browser of profMean.

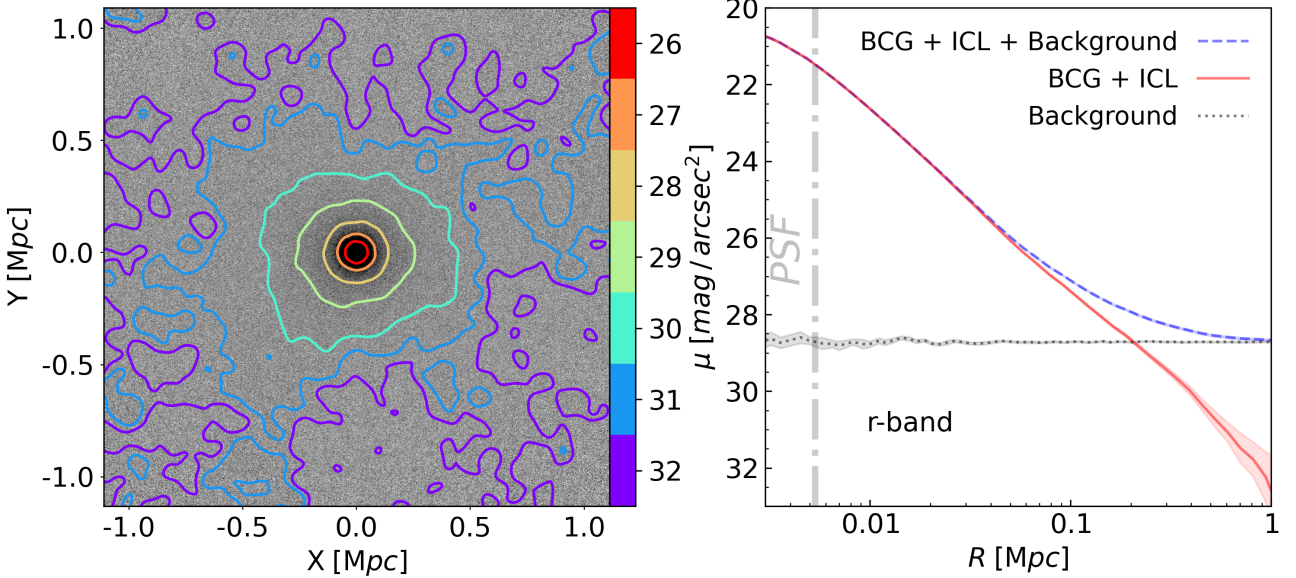


**Figure 2.** *Left:*  $r$ -band stacked 2D image of the BCG+ICL of our overall cluster sample (grayscale). Contour lines indicate the seven levels of SB ranging from 26 to 32 mag/arcsec<sup>2</sup>, colour-coded by the vertical colourbar. *Right:* SB profiles of the BCG+ICL signal (red solid), background (gray dotted), and the sum of the signal and background (blue dashed). Shaded band centered on each curve indicates the  $1\sigma$  uncertainties estimated from Jackknife resampling.

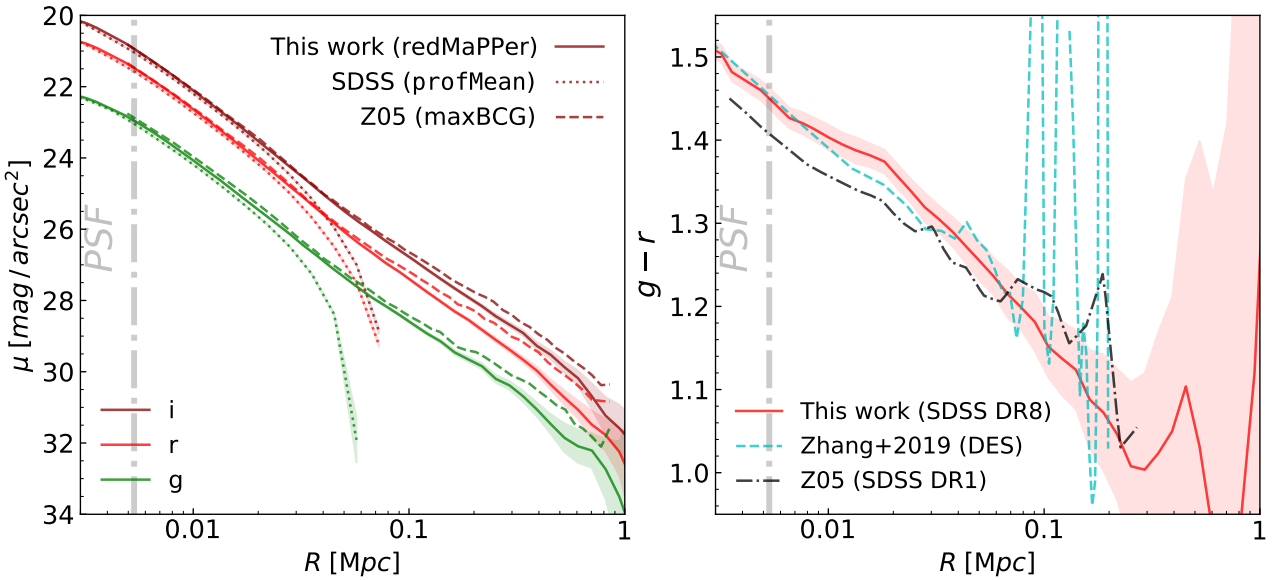


**Figure 3.** Comparison of our measurements of the BCG+ICL SB (left) and colour (right) profiles with previous studies. *Left:* Solid, dashed, and dotted curves indicate the BCG+ICL SB profiles from our measurements for redMaPPer clusters, Z05 for maxBCG clusters, and the SDSS DR7 photometric pipeline for the redMaPPer BCGs, respectively. the averaged surface brightness profile of the BCGs derived from the profMean<sup>2</sup> (which is downloaded from the SDSS Schema Browser<sup>3</sup>), respectively. Green, red, and maroon curves are the measurements for the g, r, i bands, respectively. The gray shaded region on the left roughly corresponds to the scale of PSF. *Right:* Red solid, cyan dashed, and black dot-dashed curves indicate the BCG+ICL colour profiles measured by our work from SDSS DR8, Z05 from SDSS DR1, and Zhang et al. 2019 from DES, respectively. The red shaded band represents our  $1\sigma$  uncertainties estimated from Jackknife resampling.

extended sources from outside the image boundaries, we identify all the 8 images adjacent to each target image, and apply the same masking procedure to those neighboring images. We then merge the external star and galaxy masks that overlap with the target image into the internal mask. Finally, we merge the three sets of masks from the *gri*-bands into a single image mask, so that objects below

the detection threshold in one particular band but detected in another would still be masked out in that band. By adopting a single uniform mask across three bands, we further ensure that the measurement of BCG+ICL colour profiles is robust against the discrepancy in the masks of different bandpasses..

Figure 1 demonstrates the efficacy of our masking procedure using

the *r*-band corrected frame of a typical cluster in our sample (with  $\lambda=42.6$  and  $z=0.233$ ). Each panel has a dimension of 2248 by 1689 pixels, larger than the original size of the image frame by 200 pixels on each side. Panel (a) shows the false-colour image of the cluster, with the large dashed and small solid concentric circles indicating 1 Mpc and 100 kpc-radius regions centred on the BCG, respectively. Panel (b) is similar to panel (a) but shows the *r*-band image, with the grayscale indicating the individual pixel fluxes. Panel (c) shows the masks of the detected stars (cyan solid circles), saturated pixels (black dashed circles), and galaxies (magenta solid ellipses) within the field. The circles within the white strips surrounding the original image frame represent the sources from neighboring parts of the sky. Clearly, some of the bright stars and saturated pixels in the white strips could significantly pollute pixels of the cluster image. Finally, panel (d) shows the final *r*-band image after all the masks have been applied, including those derived from the *g* and *i*-band images. We expect the fluxes within the cluster centre to be dominated by the BCG and ICL, but there still exist some unmasked satellite galaxies, faint background galaxies, and faint foreground stars in the final image of panel (d). We will statistically remove the contamination in the BCG+ICL profiles by the undetected (hence unmasked) background sources in §3.3 and faint satellites in §4.4.

### 3.2 Image Rescaling to Reference Redshift

To stack images at the same physical scale, we transform all the masked images to the reference redshift  $z_{\text{ref}}=0.25$  with the same pixel size. Firstly, we rescale the pixel size of each image by the square of the angular diameter distance ratio between the observed and reference redshifts,  $(D_A^{\text{obs}}/D_A^{\text{ref}})^2$ , and the flux within the pixel by the square of the ratio between the two luminosity distances,  $(D_L^{\text{obs}}/D_L^{\text{ref}})^2$ . Cosmic dimming is automatically included as the pixel SB varies by  $[(1+z_{\text{obs}})/(1+z_{\text{ref}})]^4$ . We do not apply any K-correction to the cluster fluxes due to the lack of robust SED templates for the ICL. However, since the reference redshift is close to the median redshift of the sample, we anticipate that the amount of K-correction in the stacked images should be largely cancelled out. In addition, we correct for Galactic extinction on the stacked profiles, rather than the individual images. Secondly, we resample all the rescaled images to 0.395''/0.396'' per pixel resolution, i.e., the original pixel size of the SDSS images. We then redistribute the image fluxes into the resampled pixels, so that the flux in each new pixel is  $\sum \mu_i A_i$ , where  $\mu_i$  is the SB of the *i*-th pixel in the rescaled image and  $A_i$  is the overlapped area between pixel *i* and that new pixel.

### 3.3 BCG+ICL SB Profile Measurement

With all clusters shifted to the reference redshift, we now stack their images centred on the BCGs in physical coordinates. We carefully account for the masked regions and adopt the mean flux at each pixel for the stacked image. A total SB profile is then computed as the azimuthally averaged SB within each annulus. However, this total SB profile includes not only the light from the BCG+ICL, but also contributions from the unmasked satellite galaxies, background galaxies, and foreground stars (i.e., BCG+ICL+Background). We will estimate the unmasked satellite contribution by inspecting the satellite stellar mass functions later in §4.4, and describe the removal of the background SB induced by the other two components below.

For any given set of clusters, we select a matching sample of

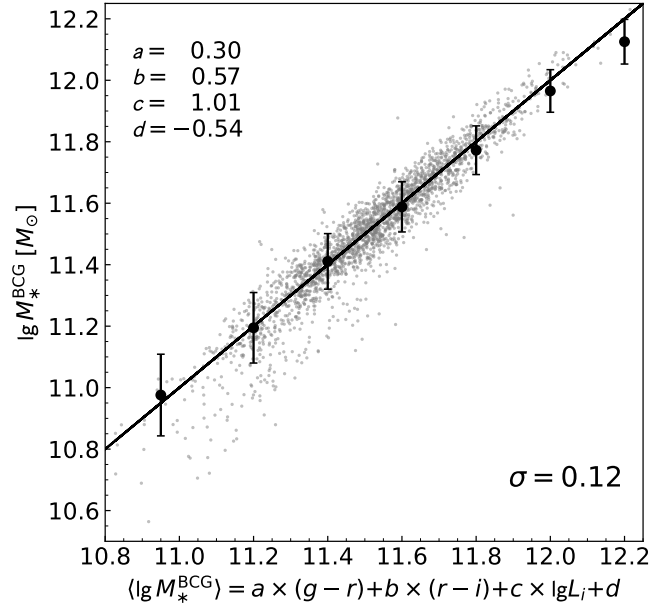


**Figure 4.** Comparison between the stellar mass-to-light ratio of BCGs measured from SPS modeling (y-axis) and that predicted by our linear estimator (x-axis). Black circles with errorbars indicate the median relation with its scatter, in good agreement with the one-to-one relation (black line). The parameters of the linear estimator are listed in the bottom right corner. [change 0.302 to 0.30](#), and likewise for the rest [Done!](#)

random clusters with the same joint distribution of redshift and richness from the SDSS redMaPPer random catalogue (v6.3) ([Rykoff et al. 2016](#)). [find the reference to the random catalogue and describe it accordingly](#) Specifically, ([Rykoff et al. 2016](#)) did this by sampling fake clusters across the entire survey volume, which shares the same richness and redshift distribution as the true cluster catalog. Firstly, pairs of  $(\lambda, z_\lambda)$  are randomly sampled from the data catalog. These pairs are assigned to a random position  $(\alpha, \delta)$ . At this step, the selected  $z_\lambda$  is compared to the maximum redshift at which the cluster can be detected (details in §3 of ([Rykoff et al. 2016](#))). This procedure will be repeated with new  $(\alpha, \delta)$  in each time until the  $z_\lambda$  is smaller than the maximum redshift at the random position. Each cluster was sampled about  $n_{\text{samp}} \sim 1000$  times to avoid the impact of noise in the random catalog on correlation measurements made on it. Thirdly, local mask fraction  $f_{\text{mask}}$  and scale factor  $\lambda/S$  are estimated based on the depth map and footprint mask. Only random points with  $f_{\text{mask}} \leq 0.2$  and  $\lambda/S \geq 20$  are left (simply as  $n_{\text{keep}}$ ), and weighted with the factor  $\omega = n_{\text{samp}}/n_{\text{keep}}$  (avoiding the impacts of survey boundary, masks, and depth variation on random points). Since the sensitivity of redMaPPer algorithm to the background is incorporated in the generation of random clusters, we expect the background SB of the random cluster images to be similar to that of the observed ones. To measure the background SB profile, we download the SDSS corrected frames that host the random clusters, and perform the same two-step quality inspection to remove defect images from the random sample. We then apply the same masking, rescaling, and stacking procedures to the random cluster images that pass the inspection, thereby producing a background SB profile for the clusters. We repeat such procedure ten times by reshuffling the relative positions of the BCGs on the images after each measurement,

and calculate the average of the ten measurements as our the final background SB profile.

Finally, we derive the BCG+ICL SB profile  $\mu^{B+I}(R)$  by subtracting the background SB profile from the total SB profile. We further normalise the  $\mu^{B+I}(R)$  profile to be zero at projected distance  $R=2$  Mpc, and focus on the SB signals at  $R < 1$  Mpc for the rest of the paper. Note that the  $\mu^{B+I}(R)$  profile measured in this way includes the contribution from the faint satellite galaxies that are unmasked. We do not subtract this contribution from our measured  $\mu^{B+I}(R)$  and  $\Sigma_*^{B+I}(R)$  profiles, but will nonetheless estimate the total stellar mass of the unmasked satellites  $\Sigma M_*^{\text{unmasked}}$  in §4.4. In order to estimate the uncertainties of  $\mu^{B+I}(R)$ , we employ the standard Jackknife resampling technique by dividing each cluster sample into 30 equal-size subsamples, and compute the error matrix from the 30 “leave-one-out” measurements (citation needed)(Efron & Stein 1981; Efron 1982). need a few sentences describing the comparison with the Z05 error measurements In Z05, they estimate the uncertainty of measurement by the rms in each radial bin. Specifically, they divided each annulus into  $n$  sectors with aperture angle  $\theta \simeq \Delta R/R$ , then used the rms among those sectors to estimate the statistical error on their average surface brightness as  $\text{rms}/\sqrt{n-1}$ . Comparing Z05 error to the estimation in this work, Z05 estimation is slightly higher within  $\sim 10$  kpc but lower beyond  $\sim 10$  kpc. The pixel number at central radii is not enough to have a good angular sector division. At radii beyond  $\sim 10$  kpc, error estimation in this work is higher than Z05  $\sim 1$  to 2 times. This difference is mainly because that Z05 estimation reflects the fluctuation in each annulus of the stacked image, while estimation in this work indicates the scatter among the 30 subsamples. Although the fraction of different images in subsamples is only a few percent, the signal beyond BCG boundaries is so weak that scatter among subsamples is larger than the fluctuation in the stacked image.

Figure 2 shows the stacked 2D image of the BCG+ICL SB distribution (left) and the corresponding SB profiles (right) for our overall cluster sample in the  $r$  band. In the left panel, the grayscale intensity represents the SB of each pixel, while the contour lines indicate seven levels of SB ranging from  $\mu = 26$  mag/arcsec $^2$  at  $R \approx 50$  kpc to 32 mag/arcsec $^2$  at  $R \approx 1$  Mpc (with  $\Delta\mu = 1$  mag/arcsec $^2$  increasing outwards), colour-coded by the vertical colorbar on the right. The azimuthally averaged 1D SB profiles are shown in the right panel, where the blue dashed, gray dotted, and red solid curves indicate the total stacked SB (BCG+ICL+background), background SB, and the BCG+ICL SB profiles  $\mu^{B+I}$ , respectively. The shaded bands indicate the SB uncertainties estimated from Jackknife resampling. Thanks to the large sample size, we are able to robustly measure the diffuse cluster light down to roughly 32 mag/arcsec $^2$  at  $R=1$  Mpc despite the relatively shallow depth of the SDSS imaging (XXXmag/arcsec $^2$  22.54mag/arcsec $^2$  in the  $i$  band).

We compare our BCG+ICL SB (left) and g-r colour (right) profiles with the results from previous studies in Figure 3. In the left panel, solid and dashed curves indicate the  $\mu^{B+I}(R)$  profiles measured for the redMaPPer clusters in this work and the maxBCG (Annis et al. 1999; Bahcall et al. 2003) clusters by Z05 cite maxbcg, respectively, in the SDSS  $g$  (green),  $r$  (red), and  $i$  (maroon) bands. The amplitudes of the maxBCG profiles are slightly higher than the redMaPPer ones on all scales, likely because the maxBCG clusters selected by Z05 are on average higher mass systems than ours. On small scales, our stacked profiles are consistent with the average BCG light profiles (dotted) derived by the SDSS photometric pipeline photo v5\_6 name and version number, but the dotted curves are rapidly cut off on scales above 30 kpc, due to the over-subtraction of the sky background on relevant scales (citation needed)(Blanton et al. 2011;

Aihara et al. 2011) I think this may be not due to sky subtraction, or sky subtraction is not the majority. In Aihara’s paper, they compare the photometric measurement on bright galaxies(i.e. the effective radius and magnitude), and they found that the improvement of the DR8 version pipeline does not work well on bright galaxies. The poor deblender may assign some of the light in the outer parts of bright galaxies to superposed fainter stars and galaxies. For the  $g-r$  color profiles shown in the right panel, our measurement (red solid) is slightly redder than the that of Z05 (black dot-dashed), consistently with the Z05 BCGs being more massive. have you corrected for reddening here? Yes We also show the DES g-r color profile measured by Zhang et al. 2019(citation needed)(Zhang et al. 2019) for the DES clusters (cyan dashed), which exhibits a simialr slope compared to Z05 and our results. The Zhang et al. profile is measured from a much smaller cluster sample than ours with  $\sim 280$  DES redMaPPer clusters, therefore their measurements are cut off at 200 kpc despite the DES photometry is roughly 2 magnitudes deeper than SDSS.

## 4 STELLAR SURFACE DENSITY PROFILE

### 4.1 Mass-to-Light Ratio

For each cluster sample, we now convert the light profiles  $\mu^{B+I}$  measured in three bands into a BCG+ICL stellar surface density profile  $\Sigma_*^{B+I}$  using an empirical method based on the template fitting described in §2.1. In particular, we assume the  $i$ -band mass-to-light ratio ( $M_*/L_i$ ) can be described by a simple linear function of the  $i$ -band luminosity  $L_i$ ,  $g-r$ , and  $r-i$  colours,

$$\lg(M_*/L_i) = a \cdot (g - r) + b \cdot (r - i) + (c - 1) \cdot \lg L_i + d. \quad (1)$$

We use  $M_*^{\text{BCG}}$ ,  $i$ -band cModel magnitudes, and the model magnitude colors of the BCGs to infer the values of  $\{a, b, c, d\}$  via least-square fitting. Figure 4 demonstrates the efficacy of our empirical calibration of  $M_*/L_i$ , where we show the distribution of BCGs on the observed vs. predicted  $M_*^{\text{BCG}}$  plane. Filled circles with errorbars indicate the mean observed  $M_*^{\text{BCG}}$  at fixed  $\langle M_*^{\text{BCG}} \rangle$  predicted by Equation 1 with  $\{a=0.30, b=0.57, c=1.01, d=-0.54\}$ , in good agreement with the one-to-one relation (solid line). The outliers in the bottom left corner mainly consist of BCGs with relatively blue colours, which have minimal impact on the least-square fit due to their small fraction.

### 4.2 Surface Density Profiles of Diffuse Light, Dark Matter, and Satellite Galaxies

In the left panel of Figure 5, we apply our best-fitting formula of  $M_*/L_i$  (Equation 1) to the  $gri$  SB profiles in Figure 3 and derive the BCG+ICL stellar surface density profile  $\Sigma_*^{B+I}(R)$  for the overall cluster sample, as shown by the open circles with errorbars. Clearly, the  $\Sigma_*^{B+I}$  profile has a significant ICL component that extends to a few  $\times 10^4 M_\odot \text{kpc}^{-2}$  at scales  $\sim 500$  kpc–1 Mpc, where we expect that the ICL largely follows the distributions of dark matter and satellite galaxies. To compare the surface density profile of the diffuse component with that of the dark matter and satellite galaxies, we show the measurements of cluster weak lensing  $\Delta\Sigma$  and galaxy number density profile  $\Sigma_g$  for the overall sample in the middle and right panels of Figure 5, respectively (squares with errorbars).

We obtain the  $\Delta\Sigma$  and  $\Sigma_g$  measurements (as well as the theoretical model of  $\Delta\Sigma$ ) by faithfully following the methods described in Z21. Briefly, the surface density contrast profile  $\Delta\Sigma(R)$  is measured from weak lensing using the DECaLS DR8 imaging, while the galaxy surface number density profile  $\Sigma_g(R)$  is calculated by

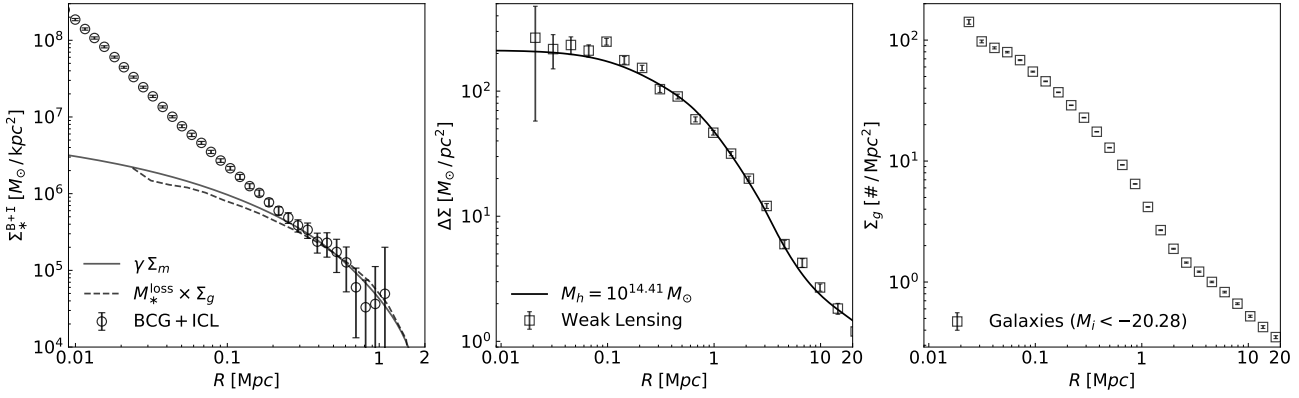


**Figure 5.** Left: Stellar surface mass density profiles. Open circles with errorbars are the  $\Sigma_*^{B+I}(R)$  profile measured in this work, while solid ( $\gamma \Sigma_m$ ) and dashed black ( $M_*^{loss} \Sigma_g$ ) curves are the model predictions assuming that the outer ICL follows the distributions of dark matter (middle panel) and satellite galaxies (right panel), respectively. Middle: Surface density contrast  $\Delta\Sigma(R)$  measured by weak lensing (squares with errorbars) and predicted by the best-fitting model described in Z21. Right: Galaxy surface number density profile  $\Sigma_g(R)$  measured from the cluster-galaxy cross-correlation function. -20.276 to -20.28 Done!

cross-correlating clusters with the photometric galaxies within SDSS DR8 ( $\text{Mag}_r < -20.28$ ). We also show the best-fitting  $\Delta\Sigma(R)$  profile predicted by the theoretical model of Z21 in the middle panel (solid curve), which describes the small-scale lensing using an NFW halo density profile with the cluster miscentring effect constrained by X-ray observations, and the large-scale lensing using a biased version of the matter clustering. From the  $\Delta\Sigma$  modelling, we infer the average halo mass of our cluster sample to be  $M_h = 10^{14.41} M_\odot$ , consistent with the results from Z21. We refer interested readers to Z21 for technical details that are beyond the scope of this paper.

Returning to the left panel of Figure 5. Solid and dashed curves show the matter surface density profile  $\Sigma_m$  and galaxy surface number density profile  $\Sigma_g$ , multiplied by a scale factor  $\gamma$  and the average mass loss per galaxy  $M_*^{loss} = 10^{10.2} M_\odot$ , respectively. In particular, the scale factor is defined as

$$\gamma(R) = \frac{\Sigma_{\text{ICL}}(R) + \Sigma_{\text{unmasked}}(R)}{\Sigma_m(R)} \quad (2)$$

where  $\Sigma_{\text{ICL}}$  is the ICL stellar mass profile and  $\Sigma_{\text{unmasked}}$  is the stellar mass profile of the unmasked satellite galaxies. By assuming that both the ICL and unmasked satellites follow the distribution of dark matter, the above equation can be simplified as

$$\gamma(R) \equiv \gamma = f_{\text{ICL}} + f_{\text{sat}}^{\text{unmasked}}, \quad (3)$$

where  $f_{\text{ICL}}$  and  $f_{\text{sat}}^{\text{unmasked}}$  are the ICL and unmasked satellite stellar-to-halo mass ratios, respectively. We infer the best-fitting values of  $\gamma = 1/419$  and  $\lg M_*^{loss} = 11.1$  by matching the scaled profiles to the  $\Sigma_*^{B+I}(R)$  measurements above  $R = 400\text{kpc}$ . We will infer the values of  $f_{\text{ICL}}$  and  $f_{\text{sat}}^{\text{unmasked}}$  separately in §4.4. Note that we predict the  $\Sigma_m$  profile from the best-fitting  $\Delta\Sigma$  model curve in the middle panel, and directly adopt the observed  $\Sigma_g$  profile in the right panel. Additionally, both curves are normalized to have zero amplitudes at  $R=2\text{Mpc}$ , following the same practice when measuring  $\Sigma_*^{B+I}$ .

Overall, the two scaled profiles  $\gamma \Sigma_m$  and  $M_*^{loss} \Sigma_g$  in the left panel of Figure 5 provide good descriptions to the BCG+ICL stellar surface density profiles at  $R > 400\text{kpc}$ , indicating that the ICL in the outer region of clusters indeed follows the distribution of the dark matter and satellite galaxies. This is consistent with the findings from (citation needed)(Montes & Trujillo 2019; Zhang et al. 2019), which suggested that the ICL is an excellent tracer of dark matter, as well as satellite stripping being the dominant channel of ICL production (citation needed)(Montes & Trujillo 2018; Jiménez-Teja et al. 2019;

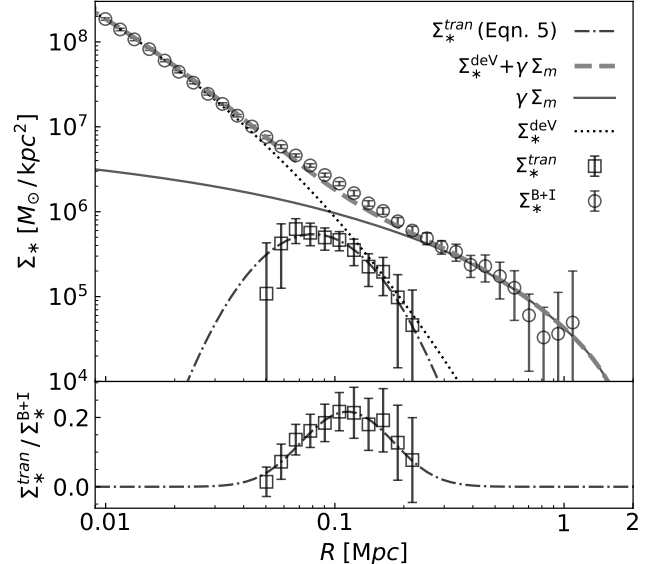


**Figure 6.** Decomposition of the BCG+ICL stellar surface mass density profile  $\Sigma_*^{B+I}$  (filled circles with errorbars). Solid curve is the total surface mass density profile  $\Sigma_m$ , scaled by a scale factor  $\gamma \equiv 1/419$  (Equation 2), while the best-fitting de Vaucouleurs profile for the  $\Sigma_*^{B+I}$  profile at  $R < 20\text{kpc}$  is shown as the dotted curve. The sum of  $\gamma \Sigma_m$  and  $\Sigma_*^{\text{dev}}$  is indicated by the dashed curve, revealing an excess mass in the observed  $\Sigma_*^{B+I}$  profile on transitional scales of  $R=50-200\text{kpc}$ . Open circles with errorbars indicate this transitional component  $\Sigma_*^{\text{tran}}$ , which can be described by a Log-normal function (Equation 7; dot-dashed).

DeMaio et al. 2015, 2018). In particular, we find that our observation of the diffuse light on scales above 400kpc can be explained if  $\sim 0.1\text{-}0.2\%$  of the total mass is in the form of ICL, and if  $\sim 10^{10} M_\odot$  of stars were stripped from each satellite galaxy into the ICL.

### 4.3 Decomposition of the BCG+ICL Surface Stellar Mass Profile

Given that the outer region of the ICL roughly follows the distribution of dark matter, we can separate the observed BCG+ICL stellar surface mass profile  $\Sigma_*^{B+I}$  into at least two physically distinct components, including one that follows the dark matter on large scales ( $R=400\text{kpc}-1\text{Mpc}$ ) and the other BCG-dominated portion on small scales ( $R<20\text{kpc}$ ). By further assuming that the *intrinsic* BCG can be described by a de Vaucouleurs' profile, the BCG-dominated portion may include a third component on transitional scales where the extended BCG envelope unfolds into the ICL. Following this philosophy, we can decompose the  $\Sigma_*^{B+I}$  profile via the following three steps. Firstly, we adopt the total surface mass profile  $\Sigma_m$  inferred from weak lensing, and multiply it by  $\gamma = 1/419$  to describe  $\Sigma_*^{B+I}$  at  $R > 400\text{kpc}$ , as was done in the left panel of Figure 5.

$$\Sigma_*^{\text{ICL}}(R) = \gamma \Sigma_m(R). \quad (4)$$

Secondly, we fit a de Vaucouleurs' profile to the  $\Sigma_*^{B+I}$  measurement on scales below  $R=20\text{kpc}$ ,

$$\Sigma_*^{\text{dev}}(R) = \Sigma_e \exp\left\{-\beta_n \left(\frac{R}{R_e}\right)^{1/n} + \beta_n\right\}. \quad (5)$$

Where  $\Sigma_e$  is the amplitude of surface mass profile,  $n=4$  is the index, and  $\beta_n=2n - 0.324$ .  $R_e$  is the effective radius. For the entire cluster sample,  $\Sigma_e=10^{7.92} M_\odot$  and  $R_e=15.4\text{kpc}$ . Finally, we subtract  $\Sigma_*^{\text{ICL}}$  and  $\Sigma_*^{\text{dev}}$  from the measured  $\Sigma_*^{B+I}$  profile, leaving us the transitional component

$$\Sigma_*^{\text{tran}}(R) = \Sigma_*^{\text{BCG+ICL}}(R) - \left[ \Sigma_*^{\text{dev}}(R) + \Sigma_*^{\text{ICL}}(R) \right]. \quad (6)$$

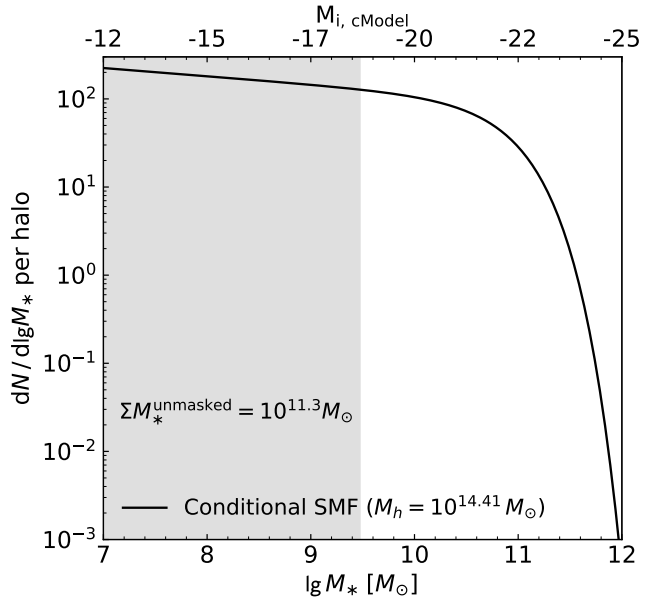
Therefore,  $\Sigma_*^{\text{tran}}(R)$  represents the excess component in the diffuse light that cannot be described by the sum of a de Vaucouleurs' profile and an ICL mass profile that follows the dark matter.

Figure 6 illustrates the physical decomposition of our observed  $\Sigma_*^{B+I}$  profile (filled circles with errorbars) into three distinct components: a de Vaucouleurs' profile  $\Sigma_*^{\text{dev}}$  (dotted curve), a scaled dark matter profile  $\Sigma_*^{\text{ICL}}$  (solid curve), and a transitional component  $\Sigma_*^{\text{tran}}$  (open circles with errorbars). The errorbars of  $\Sigma_*^{\text{tran}}$  are inherited from that of the  $\Sigma_*^{B+I}$  measurement, assuming zero uncertainties from the subtraction. Additionally, dashed curve indicates the sum of the de Vaucouleurs' profile and the scaled dark matter profile, which clearly under-predicts the signal on scales between 50kpc and 200kpc — a third component  $\Sigma_*^{\text{tran}}$  is required to fully describe the diffuse light. The ratio profile between  $\Sigma_*^{\text{tran}}(R)$  and  $\Sigma_*^{B+I}(R)$  is shown in the bottom panel of Figure 6. The transitional component accounts for more than 10% of the total diffuse mass on scales between 50kpc and 300kpc, and the ratio peaks at 35% around 100kpc. We have tested the robustness of  $\Sigma_*^{\text{tran}}(R)$  by fitting the de Vaucouleurs' profile to a larger radius at  $R = 30\text{kpc}$  or allowing the *sersic* index to vary, and the centroid and amplitude of  $\Sigma_*^{\text{tran}}(R)$  are insensitive to those changes. [check this On going!](#)

Finally, the  $\Sigma_*^{\text{tran}}(R)$  profile can be conveniently described by a Log-normal function:

$$\Sigma_*^{\text{tran}}(R) = \frac{\Sigma_0}{R \sigma_t \sqrt{2\pi}} \exp\left\{-\frac{(\ln R - \ln R_t)^2}{2\sigma_t^2}\right\}, \quad (7)$$

where  $\sigma_t=0.45$  and  $R_t=98.03\text{kpc}$  are the characteristic log-width and centroid of the transitional component, respectively. [refit the data using the new parametrization On going!](#) The best-fitting Equation 7 is shown as the dot-dashed curves in both panels of Figure 6. Although our decomposition method is physically-motivated, it depends strongly on the assumptions that the inner BCG is strictly de



**Figure 7.** Conditional satellite stellar mass function of our cluster sample (solid curve). Gray shaded region indicates the stellar mass range of satellites that are undetected by our source finding algorithm (hence unmasked). The top x-axis indicates the corresponding *i*-band cModel absolute magnitudes. The total stellar mass of the unmasked satellite galaxies is  $\Sigma M_*^{\text{unmasked}} = 2 \times 10^{11} M_\odot$ .

Vaucouleurs and the outer ICL follows the dark matter. In future work, we will investigate if a similar transitional component would emerge from the hydrosimulations after we apply our decomposition method to the simulated clusters.

### 4.4 Stellar Mass Budget of Clusters

With the physical decomposition in Figure 6, we are now ready to derive the stellar mass budget of clusters in three states: BCG, ICL, and satellite galaxies. In order to estimate the total amount of stellar mass inside the satellite galaxies, we make use of the conditional stellar mass function (CSMF) of clusters measured by Yang et al. 2012 ([citation needed](#))[\(Yang et al. 2012\)](#). In particular, we adopt the shape of the measured CSMF for the halo mass bin of  $10^{14.37}-10^{14.67} M_\odot$ , which can be described by a Schechter function

$$\Phi(M_*) = \phi_{\text{pivot}} \left(\frac{M_*}{M_{\text{pivot}}}\right)^{\alpha+1} \exp\left\{-\frac{M_*}{M_{\text{pivot}}}\right\} \quad (8)$$

with  $\lg M_{\text{pivot}}=10.92 M_\odot$  unit? and  $\alpha=-1.093$ . However, the Yang et al. CSMF was measured for a sample of galaxy groups at  $z<0.1$ , which has a different value of  $\phi_{\text{pivot}}$  than that of our cluster sample at  $z\sim0.25$ . To determine  $\phi_{\text{pivot}}$ , we compute the total number of satellite galaxies per halo above our *i*-band absolute magnitude limit of -20.28 by integrating the galaxy surface number density profile  $\Sigma_g$  to  $R=1.47\text{Mpc}$  (which is the median  $R_{200m}$  of cluster sample. Here we estimated  $R_{200m}$  based on the Mass-richness relation derived by [\(Simet et al. 2017\)](#)), as shown in the right panel of Figure 5. Given that the *i*-band magnitude of -20.28 roughly corresponds to a stellar mass of  $10^{10.2} M_\odot$  (assuming a  $M_*/L_i$  of 1.88), we normalise Equation 8 for our cluster sample by enforcing the total number of satellites above  $M_* = 10^{10.2} M_\odot$  to be 57 per halo, yielding a  $\phi_{\text{pivot}}=97.2$  per dex per halo.unit? Figure 7 shows the correctly

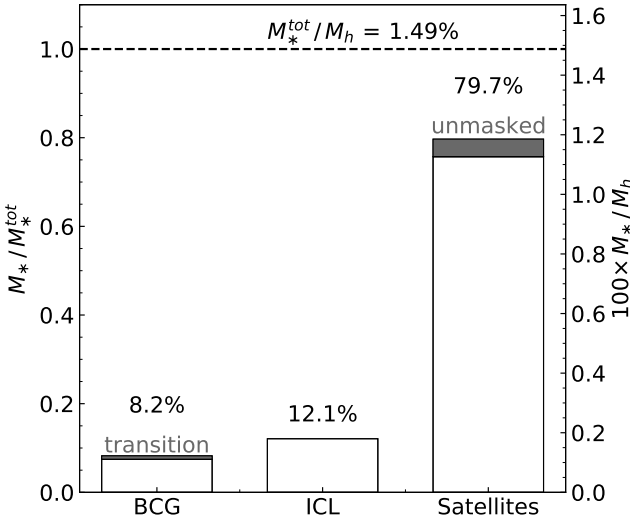


**Figure 8.** Stellar mass budget of our cluster sample in BCG, ICL, and satellites. The gray shaded portions on top of the histograms for BCG and satellites represent the contributions from the transitional component and unmasked satellites, respectively. The stellar mass fraction and stellar-to-total mass ratio of each component are indicated by the left and right y-axes, respectively. The percentage value on top of each histogram indicates the stellar mass fraction of each component, while the horizontal line indicates the total stellar-to-halo mass fraction ratio of the clusters  $M_*^{\text{tot}}/M_h$ .

normalized CSMF of our cluster sample (solid curve), which we integrate from  $M_* = 10^{9.47} M_\odot$  to  $10^{12} M_\odot$  to obtain the average stellar mass of the satellites  $\langle M_*^{\text{sat}} \rangle = 10^{10.41} M_\odot$  and the total amount of satellite stellar mass  $\Sigma M_*^{\text{sat}} = 10^{12.55} M_\odot$ .

Furthermore, the gray shaded region (below  $\lg M_* = 9.47$ ) in Figure 7 indicates the stellar mass range that is below the detection threshold of our source finding algorithm, hence unmasked during the SB measurement. This detection threshold roughly corresponds to the i-band limiting cModel magnitude of 22.08 at  $z \sim 0.25$ , i.e., an absolute magnitude of -18.49, yielding a total unmasked stellar mass of  $\Sigma M_*^{\text{unmasked}} = 2 \times 10^{11} M_\odot$ . We remove this unmasked stellar mass contribution from the ICL stellar mass budget as follows. The unmasked satellite mass fraction is  $f_{\text{sat}}^{\text{unmasked}} = \Sigma M_*^{\text{unmasked}} / M_h = 0.059\%$ . Since the scale factor defined in Equation 3 is  $\gamma = 1/419$ , we can infer the ICL mass fraction as  $f_{\text{ICL}} = \gamma - f_{\text{sat}}^{\text{unmasked}} = 1/419 - 0.00059 = 1/556$ .

Finally, Figure 8 shows the stellar mass budget of our cluster sample. We show the stellar mass fractions of the BCG, ICL, and satellites in the left y-axis, and the stellar-to-halo mass fractions of the three components in the right y-axis. The “transition” portion indicates the integrated mass within the  $\Sigma_*^{\text{tran}}$  profile ( $10^{10.57} M_\odot$ ) shown in Figure 6, while the “unmasked” portion corresponds to the gray shaded region in Figure 7. The dashed horizontal line in the top indicates the total stellar mass-to-halo mass ratio (1.49%) assuming a halo mass of  $10^{14.49} M_\odot$  measured from weak lensing in Z21, significantly below the cosmic baryon fraction of 15.74% (under the adopted cosmology). Assuming further that the total baryon fraction of the clusters is the cosmic value  $f_b = \Omega_b/\Omega_m$  (citation needed)(Planck Collaboration et al. 2016), we can infer that the 90.4% of the baryons are in the form of the hot gas within clusters. For the stellar mass budget, 79.7% of the stellar mass is inside the

satellite galaxies, while 8.2% is in the BCG, leaving 12.1% of the stellar mass in the diffuse form of free-floating stars.

**compare to the ICL numbers in the literature** In observation, the ICL mass fraction in this work is consistent with the analysis of (Morishita et al. 2017). In (Morishita et al. 2017), they measured the ICL color and mass profiles of the six Hubble Frontier Field clusters with the deep *Hubble Space Telescope (HST)* imaging data. Their result shows that the ICL stellar mass is  $10^{11}$  to  $10^{12} M_\odot$  and is about 5% to 20% of the total cluster stellar mass.

## 5 $R_{\text{SOI}}$ : SPHERE OF INFLUENCE OF THE BCG

Although we tentatively assign the transitional component to the BCG in Figure 8, it is unclear whether this stellar mass excess is primarily induced by the BCG or the richness. Despite accounting only for 4% of the total stellar mass, this transitional component is key to solving the sphere of influence of the BCGs  $R_{\text{SOI}}$ . In particular, if the excess mass is primarily richness-induced, we expect  $R_{\text{SOI}}$  to stop at  $\sim 50$ kpc; but a BCG-induced origin would extend  $R_{\text{SOI}}$  beyond the transitional component at  $\sim 200$ kpc. In this section, we divide our overall cluster sample into two subsamples of different average BCG stellar mass  $M_*^{\text{BCG}}$ , and aim to distinguish the two physical scenarios by comparing the two sets of diffuse light and mass profiles.

### 5.1 Cluster Subsamples Split by $M_*^{\text{BCG}}$

Following Z21, we split the clusters into two subsamples using the median  $M_*^{\text{BCG}} - \lambda$  relation, illustrated by the top left panel in Figure 9. In particular, the median  $M_*^{\text{BCG}} - \lambda$  relation (solid line) can be described by

$$\langle \lg M_*^{\text{BCG}} \rangle = 0.45 \lg \lambda + 10.86 \quad (9)$$

dividing the clusters into two halves with the same distribution of satellite richness  $\lambda$ , which we refer to simply as the “high- $M_*^{\text{BCG}}$ ” and “low- $M_*^{\text{BCG}}$ ” subsamples for the rest of the paper. By applying the methods described in §3 and §4, we measure the BCG+ICL surface brightness profile  $\mu^{\text{B+I}}$  (top middle panel) and stellar surface mass profile  $\Sigma_*^{\text{B+I}}$  (top right panel) for each of the two subsamples.

In the top middle panel of Figure 9, solid and dashed curves indicate the  $\mu^{\text{B+I}}(R)$  profiles of the high and low- $M_*^{\text{BCG}}$  subsamples, respectively, in the SDSS *g* (green), *r* (red), and *i* (maroon) bands. By construction, the  $\mu^{\text{B+I}}(R)$  profile of the high- $M_*^{\text{BCG}}$  subsample is  $\sim 0.56$  magnitudes brighter than that of the low- $M_*^{\text{BCG}}$  one on scales well below the effective cModel aperture, i.e.,  $R_* = 50$ kpc, because the average  $M_*^{\text{BCG}}$  of the two subsamples differ by  $\sim 0.28$  dex. However, the small-scale discrepancy between the two subsamples persist on scales much larger than  $R_*$ , and the two sets of  $\mu^{\text{B+I}}$  profiles do not converge within the uncertainties until  $R \sim 300$ kpc. Likewise, the two  $\Sigma_*^{\text{B+I}}$  profiles in the top right panel exhibit a significant discrepancy on scales as large as  $R \sim 200$ –300kpc, beyond which they start to converge to the same level of stellar surface mass density.

The comparison between the two  $\Sigma_*^{\text{B+I}}$  profiles is better illustrated in the bottom of the top right panel of Figure 9, where we show the  $\Sigma_*^{\text{B+I}}$  ratios of the low (red solid) and high (blue dashed)  $M_*^{\text{BCG}}$  subsamples over the overall sample. The discrepancy between the two ratio profiles is approximately a factor of two (0.3 dex) across all scales below  $R = 100$ kpc before declining slowly on larger scales, but still persists at  $\sim 30\%$  level at  $R \sim 200$ –300kpc. Not until distances exceed  $R \sim 300$ kpc do the two ratio profiles begin to converge to unity (albeit with large errorbars).

Such discrepancy observed between the two subsamples provides

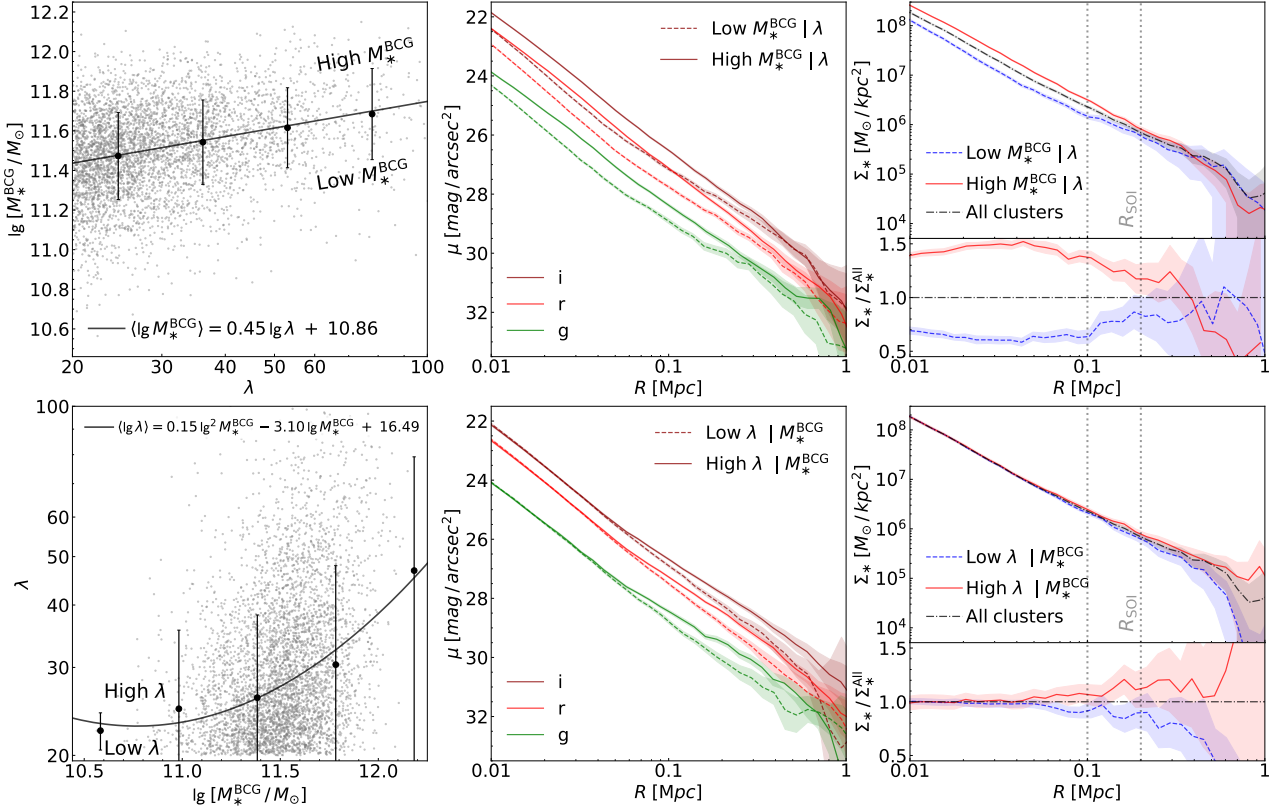


**Figure 9.** Selection method (left), surface brightness profiles (middle), and stellar surface density profiles (right) of cluster subsamples split by  $M_*^{\text{BCG}}$  (top row) and  $\lambda$  (bottom row). *Top left:* Distribution of clusters on the  $M_*^{\text{BCG}}$  vs.  $\lambda$  plane (gray dots). Black solid line is a linear fit to the median  $\lg M_*^{\text{BCG}}$  at fixed  $\lambda$ , which divides the clusters into low and high- $M_*^{\text{BCG}}$  subsamples. *Top middle:* Surface brightness profiles  $\mu^{\text{B+I}}$  of the low (dashed curves) and high (solid curves)  $M_*^{\text{BCG}}$  subsamples. Green, red, and maroon curves indicate the measurements from  $g$ ,  $r$ , and  $i$ -band images. *Top right:* Stellar surface density profiles  $\Sigma_*^{\text{B+I}}$  of the low- $M_*^{\text{BCG}}$  (blue dashed), high- $M_*^{\text{BCG}}$  (red solid), and all (gray dot-dashed) clusters. The bottom subpanel shows the ratios of the  $\Sigma_*^{\text{B+I}}$  profiles of the low (blue dashed) and high (red solid)  $M_*^{\text{BCG}}$  subsamples over that of the overall sample. The panels in the bottom row are similar, but for the subsamples split by  $\lambda$  at fixed  $M_*^{\text{BCG}}$ .

a clear detection of the BCG sphere of influence. Since the two subsamples of clusters have the same richness and differ solely in their BCG stellar mass, the clear transition from the constant discrepancy below  $R=100\text{kpc}$  to the apparent convergence above  $300\text{kpc}$  in the top right panel of Figure 9 demonstrates that the BCG sphere of influence extends to scales around  $R_{\text{SOI}} \sim 200\text{kpc}$ . Interestingly, such transition at  $R_{\text{SOI}}$  coincides with the radial extent of the transitional stellar mass component revealed by the  $\Sigma_*^{\text{B+I}}$  decomposition in §4.3, suggesting a common origin of the two observed ‘‘transitions’’. In particular, the excess diffuse light on scales between  $R_*$  and  $R_{\text{SOI}}$  should be primarily formed via processes that simultaneously enriched the BCG, likely due to the tidal disruption/stripping of satellites after periapsis and the stellar ejection from mergers between the BCGs and satellites. Furthermore, the convergence of the two  $\Sigma_*^{\text{B+I}}$  profiles on scales above  $300\text{kpc}$  confirms our expectation that the ICL in the outer region of clusters largely follows the distribution of satellite galaxies, hence that of the dark matter.

The bottom panels of Figure 9 shows the results of a similar experiment as in the top panels, but by dividing the clusters into low and high- $\lambda$  subsamples by the richness  $\lambda$  at fixed BCG stellar mass  $M_*^{\text{BCG}}$  (bottom left panel). As expected, the two sets of  $\mu^{\text{B+I}}$  and  $\Sigma_*^{\text{B+I}}$  profiles are consistent on scales below  $R_* = 50\text{kpc}$ , but start to differ on scales above, reaching a discrepancy of 20% at  $R \sim 200\text{kpc}$ . Overall, the discrepancy between the low and high- $\lambda$

clusters is significantly smaller than that between the two  $M_*^{\text{BCG}}$ -split halves on scales between  $50\text{kpc}$  and  $200\text{kpc}$ , indicating that the influence of satellite richness is subdominant compared to the BCG on those transitional scales — they are firmly within the sphere of influence of the BCG.

Figure 10 provides a more visually-appealing way of comparing the diffuse light distributions between the low and high- $M_*^{\text{BCG}}$  subsamples. In particular, we compare the 2D stacked  $r$ -band images of the low- $M_*^{\text{BCG}}$  (left) and high- $M_*^{\text{BCG}}$  (right) subsamples (dashed contours) to that of the overall sample (solid contours in both panels; same as in Figure 2). Consistent with 1D profiles in the top panels of Figure 9, the high- $M_*^{\text{BCG}}$  clusters exhibits a more enhanced surface brightness distribution than the low- $M_*^{\text{BCG}}$  systems on scales below  $300\text{kpc}$ , but the two images are almost indistinguishable on scales above  $500\text{kpc}$ .

## 5.2 Systematic Tests Against Stellar Mass Aperture and BCG Centering Probability

The key conclusion of our paper, that the BCG sphere of influence extends to a characteristic radius of  $R_{\text{SOI}} \approx 200\text{kpc}$ , is based on the experiments of § 5.1. However, the experiments could be affected by systematic uncertainties associated with the aperture of our stellar mass estimates or the miscentering effect in the redMaPPer cluster

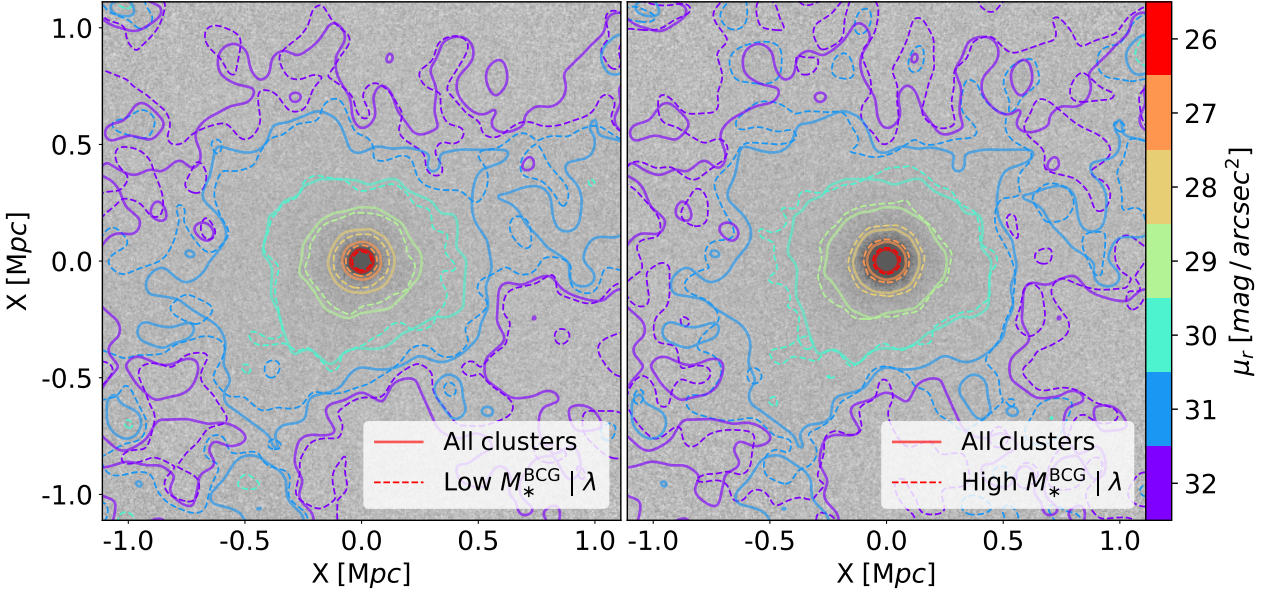


**Figure 10.** Comparison of the  $r$ -band stacked 2D image of the low (left) and high (right)  $M_*^{\text{BCG}}$  subsamples. In each panel, dashed contour lines show the surface brightness distribution of the subsample, while the solid contours are for the overall sample, with the same colour-coding as in Figure 2. Below  $\sim 300\text{kpc}$ , the SB distribution of the low- $M_*^{\text{BCG}}$  subsample is generally fainter than that of the overall sample, which is then fainter than that of the high- $M_*^{\text{BCG}}$  subsample. On scales above  $\sim 500\text{kpc}$ , the three sets of contours are roughly consistent with one another.

finding algorithm (citation needed)(Johnston et al. 2007; Oguri & Takada 2011; Rozo & Rykoff 2014; Hollowood et al. 2019). For example, although the effective aperture of  $M_*^{\text{BCG}}$  is  $R_* \sim 50\text{kpc}$ , the individual apertures of some of the nearby, bright systems could be larger, thereby artificially pushing the discrepancy between the  $\Sigma_*^{\text{B+I}}$  of high and low- $M_*^{\text{BCG}}$  subsample to larger radii. For miscentring, the average centring probability  $p_{\text{cen}}$  of the low- $M_*^{\text{BCG}}$  clusters is lower, and is thus more likely to have satellite galaxies misidentified as centrals than their high- $M_*^{\text{BCG}}$  counterparts. Consequently, it is plausible that the  $\Sigma_*^{\text{B+I}}$  of the low- $M_*^{\text{BCG}}$  subsample is heavily underestimated on small scales due to the lack of extended stellar envelope surrounding those misidentified centrals.

To investigate the impact of different apertures, we repeat the experiment of § 5.1 by adopting  $M_{*,20\text{kpc}}$ , the stellar mass measured within a fixed aperture of 20kpc. By splitting the clusters into two subsamples of different  $M_{*,20\text{kpc}}$  at fixed  $\lambda$ , we eliminate the possibility that the high- $msbcg$  subsample may preferentially select the larger BCGs. The result of this test is shown as the red (high- $M_{*,20\text{kpc}}$ ) and blue (low- $M_{*,20\text{kpc}}$ ) dashed curves in Figure 11. The  $\Sigma_*^{\text{B+I}}$  of the high- $M_{*,20\text{kpc}}$  subsample is  $\sim 2.6$  per cent lower than that of the high- $M_*^{\text{BCG}}$  clusters on scales below 200kpc, while the  $\Sigma_*^{\text{B+I}}$  of the low- $M_{*,20\text{kpc}}$  subsample is largely consistent with that of the low- $M_*^{\text{BCG}}$  clusters on all scales. While the  $\Sigma_*^{\text{B+I}}$  of the low- $M_{*,20\text{kpc}}$  subsample is  $\sim 2.1$  per cent higher than that of the low- $M_*^{\text{BCG}}$  subsample. Overall, the discrepancy between the  $\Sigma_*^{\text{B+I}}$  profiles of the two subsamples split by  $M_{*,20\text{kpc}}$  is very similar to our fiducial measurement split by  $M_*^{\text{BCG}}$  (solid curves), consistent with the BCG sphere of influence extending to  $R_{\text{SOI}} \sim 200\text{kpc}$ .

To test the miscentring effect, we measure the  $p_{\text{cen}}$  distributions of the BCGs of the high (red histograms) and low (blue histograms)  $M_*^{\text{BCG}}$  subsamples in the inset panel of Figure 11. Both  $p_{\text{cen}}$  distributions peak close to 100%, but the distribution of the low- $M_*^{\text{BCG}}$  clusters indeed exhibits a longer low- $p_{\text{cen}}$  tail. To eliminate the impact of low- $p_{\text{cen}}$  systems on our  $R_{\text{SOI}}$  measurement, we remove

clusters with the  $p_{\text{cen}}$  of their BCGs lower than 85%, shown as the vertical dashed line in the inset panel, and redo the analysis using the  $M_*^{\text{BCG}}$ -split subsamples. The results of the miscentring test are shown by the red and blue dotted curves for the high and low- $M_*^{\text{BCG}}$  clusters with  $\text{BCg } p_{\text{cen}} > 85\%$ , respectively. Again, we do not find any significant deviation from our fiducial measurements due to the exclusion of the low- $p_{\text{cen}}$  systems.

Therefore, based on the two systematic tests shown in Figure 11, we conclude that the detection of  $R_{\text{SOI}} \sim 200\text{kpc}$  is robust against the aperture size of the BCG stellar mass estimates and the level of miscentring in the SDSS redMaPPer catalogue.

### 5.3 Connection between BCG Sphere of Influence and Halo Concentration

As mentioned in the Introduction, Z21 modelled the weak lensing measurements of the two subsamples split by  $M_*^{\text{BCG}}$  at fixed  $\lambda$ , and found that the two have the same average halo mass, but the average halo concentration of the high- $M_*^{\text{BCG}}$  clusters is  $\sim 10\%$  higher than that of the low- $M_*^{\text{BCG}}$  systems (for a thorough explanation of such observation, see Zu et al. 2021b (citation needed)(Zu et al. 2021a)

Zu et al. 2021a cannot change after compiling). Z21 speculated that the strong correlation between halo concentration and  $M_*^{\text{BCG}}$  could be induced at the early phase of halo growth, when the fast accretion and frequent mergers not only built the characteristic cores of the cluster haloes, but also fuel the *in situ* stellar growth of the BCGs. Interestingly, the characteristic radii  $r_s$  inferred by Z21 are  $\sim 200\text{--}300\text{kpc}$ , in good agreement with our constraint of  $R_{\text{SOI}}$  in this paper.

Such similarity between the values of  $r_s$  and  $R_{\text{SOI}}$  is likely physical. In the vicinity of the BCGs, stars could be tidally disrupted/stripped from satellites after periapsis or ejected from BCG-satellite mergers. Most of those stray stars cannot escape to larger radii due to the relatively high escape velocities within  $r_s$ . Therefore,

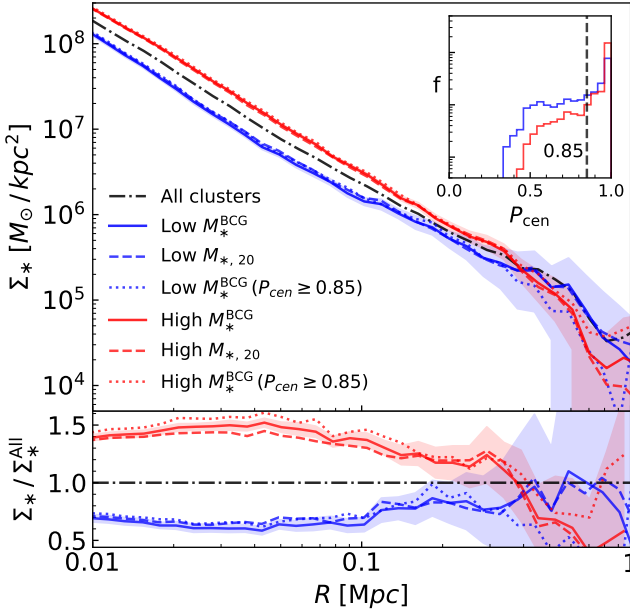


**Figure 11.** Similar to the top right panel of Figure 9, but with measurements for cluster subsamples split by  $M_{*,20\text{kpc}}$  (stellar mass measured within a 20kpc aperture; dashed curves) and for clusters with BCG centring probability  $p_{\text{cen}} > 0.85$  (dotted curves). Inset panel shows the  $p_{\text{cen}}$  distributions of the low (blue histograms) and high (red histograms)  $M_{*}^{\text{BCG}}$  subsamples, with the vertical dashed line indicating our  $p_{\text{cen}}=0.85$  cut.

a fraction of them would fall back onto the BCGs and grow  $M_{*}^{\text{BCG}}$ , while the rest stays unbound to the BCGs and form the transitional component  $\Sigma_{*}^{\text{tran}}$ , which is however well confined within the BCG sphere of influence  $R_{\text{SOI}}$ . In this scenario, the BCG sphere of influence is partly maintained by the central core of the halo. Future observations with even larger cluster samples and deeper photometry could potentially clarify the existence of this  $r_s$ - $R_{\text{SOI}}$  connection.

Finally, we present a comprehensive comparison between the low (blue squares) and high (red circles)  $M_{*}^{\text{BCG}}$  subsamples in their BCG+ICL stellar surface density profiles  $\Sigma_{*}^{\text{B+I}}$  (left), weak lensing profiles  $\Delta\Sigma$  (middle), and galaxy surface number density profile  $\Sigma_g$  (right) in Figure 12. The left panel is similar to Figure 6, but with our decomposition method applied to the two subsamples separately. The integrated mass within the transitional component  $\Sigma_{*}^{\text{tran}}$  of the high- $M_{*}^{\text{BCG}}$  subsample (red filled circles) is  $10^{10.82} M_{\odot}$ , ~0.27 dex higher than that of the low- $M_{*}^{\text{BCG}}$  subsample (blue filled squares), consistent?larger?smaller?smaller with the 0.28 dex discrepancy between the two average  $M_{*}^{\text{BCG}}$ .

The middle panel of Figure 12 is similar to the Figure 5 of Z21, showing the weak lensing comparison between the two subsamples. We also include the weak lensing signals predicted on small scales by the de Vaucouleurs' profiles of the BCGs (dotted curves) in the prediction of the total  $\Delta\Sigma$  (dashed curves). The 10% difference in halo concentration is manifested by the large discrepancy between the two  $\Delta\Sigma$  profiles on scales between 100kpc and 500kpc. We show the comparison between the two galaxy surface number density profiles in the right panels of Figure 12 (similar to the right panel of Figure 6 in Z21). Clearly, the galaxy distributions around the BCGs of the two subsamples are almost indistinguishable, indicating that the differences in  $\Sigma_{*}^{\text{B+I}}$  (left) and  $\Delta\Sigma$  (middle) are tied solely to the discrepancy in  $M_{*}^{\text{BCG}}$ . The remarkable similarity between the two  $\Sigma_g$

profiles also confirms our expectation that the richness-induced ICL profiles between the two subsamples should be the same.

## 6 CONCLUSION

### DATA AVAILABILITY

The data underlying this article will be shared on reasonable request to the corresponding author.

### ACKNOWLEDGEMENTS

We thank XXX for helpful discussions. XKC and YZ acknowledge the support by the National Key Basic Research and Development Program of China (No. 2018YFA0404504), National Science Foundation of China (11873038, 11621303, 11890692), and the science research grants from the China Manned Space Project (No. CMS-CSST-2021-A01, CMS-CSST-2021-B01). YZ acknowledges the National One-Thousand Youth Talent Program of China, the SJTU start-up fund (No. WF220407220), and the support by the 111 Project of the Ministry of Education under grant No. B20019. YZ thanks the wonderful hospitality by Cathy Huang during his visit at the Zhangjiang Hi-Tech Park during the summer of 2021.

### REFERENCES

- Aihara H., et al., 2011, *ApJS*, **193**, 29
- Akeson R., et al., 2019, arXiv e-prints, p. [arXiv:1902.05569](https://arxiv.org/abs/1902.05569)
- Alonso Asensio I., Dalla Vecchia C., Bahé Y. M., Barnes D. J., Kay S. T., 2020, *MNRAS*, **494**, 1859
- Annis J., et al., 1999, in American Astronomical Society Meeting Abstracts. p. 12.02
- Bahcall N. A., et al., 2003, *ApJS*, **148**, 243
- Bernardi M., Meert A., Sheth R. K., Vikram V., Huertas-Company M., Mei S., Shankar F., 2013, *MNRAS*, **436**, 697
- Bertin E., Arnouts S., 1996, *A&AS*, **117**, 393
- Blanton M. R., Kazin E., Muna D., Weaver B. A., Price-Whelan A., 2011, *AJ*, **142**, 31
- Burke C., Collins C. A., Stott J. P., Hilton M., 2012, *MNRAS*, **425**, 2058
- Burke C., Hilton M., Collins C., 2015, *MNRAS*, **449**, 2353
- Chen Y.-M., et al., 2012, *MNRAS*, **421**, 314
- Conroy C., Wechsler R. H., Kravtsov A. V., 2007, *ApJ*, **668**, 826
- Contini E., 2021, *Galaxies*, **9**, 60
- Contini E., De Lucia G., Villalobos Á., Borgani S., 2014, *MNRAS*, **437**, 3787
- Contini E., Yi S. K., Kang X., 2018, *MNRAS*, **479**, 932
- Contini E., Yi S. K., Kang X., 2019, *ApJ*, **871**, 24
- Cooper A. P., Gao L., Guo Q., Frenk C. S., Jenkins A., Springel V., White S. D. M., 2015, *MNRAS*, **451**, 2703
- Cui W., et al., 2014, *MNRAS*, **437**, 816
- DeMaio T., Gonzalez A. H., Zabludoff A., Zaritsky D., Bradač M., 2015, *MNRAS*, **448**, 1162
- DeMaio T., Gonzalez A. H., Zabludoff A., Zaritsky D., Connor T., Donahue M., Mulchaey J. S., 2018, *MNRAS*, **474**, 3009
- Dolag K., Murante G., Borgani S., 2010, *MNRAS*, **405**, 1544
- Donzelli C. J., Muriel H., Madrid J. P., 2011, *ApJS*, **195**, 15
- Efron B., 1982, The Jackknife, the Bootstrap and other resampling plans
- Efron B., Stein C., 1981, *The Annals of Statistics*, **9**, 586
- Furnell K. E., et al., 2021, *MNRAS*, **502**, 2419
- Gong Y., et al., 2019, *ApJ*, **883**, 203
- Gonzalez A. H., Zabludoff A. I., Zaritsky D., 2005, *ApJ*, **618**, 195
- Gu M., et al., 2020, *ApJ*, **894**, 32
- Han S., Smith R., Choi H., Cortese L., Catinella B., Contini E., Yi S. K., 2018, *ApJ*, **866**, 78

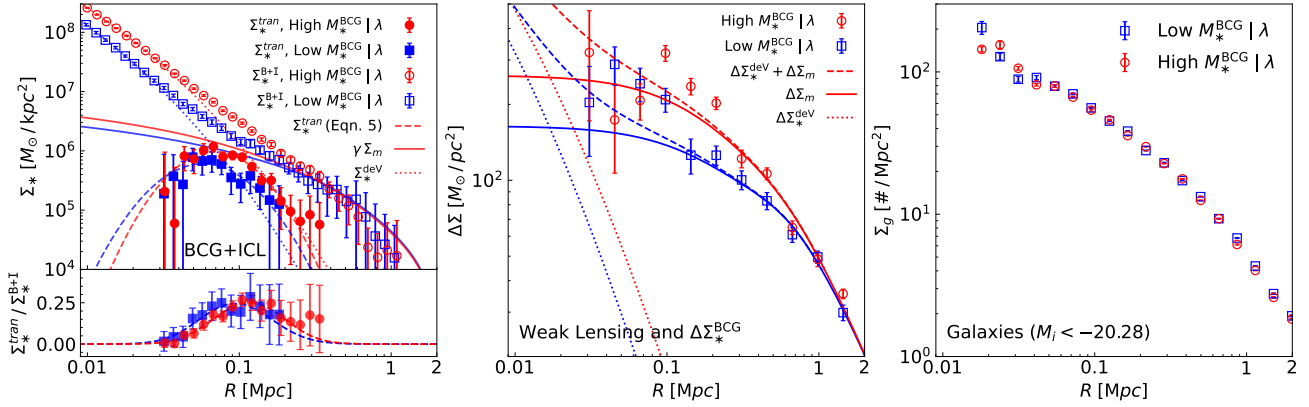


**Figure 12.** *Left:* BCG+ICL stellar surface density profiles  $\Sigma_*^{B+I}$  of the low (blue open squares) and high (red open circles)  $M_*^{BCG}$  subsamples. Solid and dotted curves are the best-fitting scaled matter density and de Vaucouleurs' profiles on relevant scales, respectively. Blue filled squares and red filled circles indicate the transitional components of the low and high- $M_*^{BCG}$  clusters, respectively, while the dashed curves are the best-fitting log-normal functions. *Middle:* Weak lensing profiles  $\Delta\Sigma$  of the low (blue open squares) and high (red open circles)  $M_*^{BCG}$  subsamples. Solid curves are the predictions by the best-fitting  $\Delta\Sigma$  models described in Z21. The two  $\Delta\Sigma$  models have the same halo mass, but the average halo concentration of the high- $M_*^{BCG}$  subsample is  $\sim 10\%$  higher than that of the low- $M_*^{BCG}$  clusters. Dotted curves indicate the predicted  $\Delta\Sigma$  signal induced by the respective de Vaucouleurs' profiles shown in the left panel, and each dashed curve is the sum of the dotted and solid curves of the same colour. *Right:* The galaxy surface number density profiles  $\Sigma_g$  of the low (blue open squares) and high (red open circles)  $M_*^{BCG}$  subsamples. The two measured profiles are consistent with each other on all scales.

- Hollowood D. L., et al., 2019, *ApJS*, **244**, 22  
 Huang S., et al., 2021, arXiv e-prints, p. arXiv:2109.02646  
 Ivezić Ž., et al., 2019, *ApJ*, **873**, 111  
 Jiménez-Teja Y., et al., 2018, *ApJ*, **857**, 79  
 Jiménez-Teja Y., et al., 2019, *A&A*, **622**, A183  
 Johnston D. E., et al., 2007, arXiv e-prints, p. arXiv:0709.1159  
 Kluge M., Bender R., Riffeser A., Goessl C., Hopp U., Schmidt M., Ries C., 2021, *ApJS*, **252**, 27  
 Kravtsov A. V., Vikhlinin A. A., Meshcheryakov A. V., 2018, *Astronomy Letters*, **44**, 8  
 Mancone C. L., Gonzalez A. H., 2012, *PASP*, **124**, 606  
 Maraston C., Strömbäck G., Thomas D., Wake D. A., Nichol R. C., 2009, *MNRAS*, **394**, L107  
 Martel H., Barai P., Brito W., 2012, *ApJ*, **757**, 48  
 Melnick J., Giraud E., Toledo I., Selman F., Quintana H., 2012, *MNRAS*, **427**, 850  
 Mihos J. C., Harding P., Feldmeier J., Morrison H., 2005, *ApJ*, **631**, L41  
 Mihos J. C., Harding P., Feldmeier J. J., Rudick C., Janowiecki S., Morrison H., Slater C., Watkins A., 2017, *ApJ*, **834**, 16  
 Montes M., Trujillo I., 2014, *ApJ*, **794**, 137  
 Montes M., Trujillo I., 2018, *MNRAS*, **474**, 917  
 Montes M., Trujillo I., 2019, *MNRAS*, **482**, 2838  
 Montes M., Brough S., Owers M. S., Santucci G., 2021, *ApJ*, **910**, 45  
 Morishita T., Abramson L. E., Treu T., Schmidt K. B., Vulcani B., Wang X., 2017, *ApJ*, **846**, 139  
 Murante G., Giovalli M., Gerhard O., Arnaboldi M., Borgani S., Dolag K., 2007, *MNRAS*, **377**, 2  
 Navarro J. F., Frenk C. S., White S. D. M., 1996, *ApJ*, **462**, 563  
 Oguri M., Takada M., 2011, *Phys. Rev. D*, **83**, 023008  
 Planck Collaboration et al., 2016, *A&A*, **594**, A13  
 Poliakov D., Mosenkov A. V., Brosch N., Koriski S., Rich R. M., 2021, *MNRAS*, **503**, 6059  
 Presotto V., et al., 2014, *A&A*, **565**, A126  
 Puchwein E., Springel V., Sijacki D., Dolag K., 2010, *MNRAS*, **406**, 936  
 Purcell C. W., Bullock J. S., Zentner A. R., 2007, *ApJ*, **666**, 20  
 Rozo E., Rykoff E. S., 2014, *ApJ*, **783**, 80  
 Rudick C. S., Mihos J. C., McBride C., 2006, *ApJ*, **648**, 936  
 Rudick C. S., Mihos J. C., Frey L. H., McBride C. K., 2009, *ApJ*, **699**, 1518  
 Rudick C. S., Mihos J. C., McBride C. K., 2011, *ApJ*, **732**, 48  
 Rykoff E. S., et al., 2014, *ApJ*, **785**, 104  
 Rykoff E. S., et al., 2016, *ApJS*, **224**, 1  
 Seigar M. S., Graham A. W., Jerjen H., 2007, *MNRAS*, **378**, 1575  
 Simet M., McClintock T., Mandelbaum R., Rozo E., Rykoff E., Sheldon E., Wechsler R. H., 2017, *MNRAS*, **466**, 3103  
 Spergel D., et al., 2015, arXiv e-prints, p. arXiv:1503.03757  
 Tang L., Lin W., Cui W., Kang X., Wang Y., Contini E., Yu Y., 2018, *ApJ*, **859**, 85  
 Willman B., Governato F., Wadsley J., Quinn T., 2004, *MNRAS*, **355**, 159  
 Yang X., Mo H. J., van den Bosch F. C., Zhang Y., Han J., 2012, *ApJ*, **752**, 41  
 York D. G., et al., 2000, *AJ*, **120**, 1579  
 Zhang Y., et al., 2019, *ApJ*, **874**, 165  
 Zibetti S., White S. D. M., Schneider D. P., Brinkmann J., 2005, *MNRAS*, **358**, 949  
 Zu Y., et al., 2021a, arXiv e-prints, p. arXiv:2108.06790  
 Zu Y., et al., 2021b, *MNRAS*, **505**, 5117  
 Zwicky F., 1937, *ApJ*, **86**, 217  
 Zwicky F., 1952, *PASP*, **64**, 242

## REFERENCES

This paper has been typeset from a  $\text{\TeX}/\text{\LaTeX}$  file prepared by the author.